

# Electronic structure, phase stability, and transport properties of the AlTiVCr lightweight high-entropy alloy: A computational study

Christopher D. Woodgate,<sup>1,\*</sup> Hubert J. Naguszewski,<sup>2</sup> Nicolas F. Piwek,<sup>3</sup> and David Redka<sup>3,4</sup>

<sup>1</sup>*H.H. Wills Physics Laboratory, University of Bristol, Royal Fort, Bristol, BS8 1TL, United Kingdom*

<sup>2</sup>*Department of Physics, University of Warwick, Coventry, CV4 7AL, United Kingdom*

<sup>3</sup>*Lasercenter HM, Munich University of Applied Sciences HM, Lothstraße 34, 80335 Munich, Germany*

<sup>4</sup>*New Technologies Research Centre, University of West Bohemia, Univerzitní 8, 30100 Pilsen, Czech Republic*

(Dated: January 23, 2026)

We investigate the thermodynamics and phase stability of the AlTiVCr lightweight high-entropy alloy using a combination of *ab initio* electronic structure calculations, a concentration wave analysis, and atomistic Monte Carlo simulations. In alignment both with experimental data and with results obtained using other computational approaches, we predict a B2 (CsCl) chemical ordering emerging in this alloy at comparatively high temperatures, which is driven by Al and Ti moving to separate sublattices, while V and Cr express weaker site preferences. The impact of this B2 chemical ordering on the electronic transport properties of the alloy is investigated within a Kubo–Greenwood linear response framework and it is found that, counter-intuitively, the alloy’s residual resistivity increases as the material transitions from the A2 (disordered bcc) phase to our predicted B2 (partially) ordered structure. This is understood to result primarily from a reduction in the density of electronic states at the Fermi level induced by the chemical ordering. At low temperatures, our atomistic Monte Carlo simulations then reveal subsequent sublattice orderings, with the ground-state configuration predicted to be a fully-ordered single-phase structure with vanishing associated residual resistivity. These results give fresh, insight into the atomic-scale structure and consequent physical properties of this well-studied, technologically relevant material.

## I. INTRODUCTION

Though now first reported more than twenty years ago by Yeh *et al.* [1] and Cantor *et al.* [2], high-entropy alloys (HEAs)—single-phase alloys combining four or more elements in near-equal ratios—continue to attract significant attention in the field of materials science [3, 4]. These materials, also sometimes referred to as ‘complex concentrated’ or ‘multi-principle element’ alloys, are of interest for a range of advanced engineering applications because they frequently exhibit superior physical properties as compared to traditional binary/ternary alloys, including impressive fracture resistance [5–7] and corrosion resistance [8], good radiation damage tolerance [9, 10], and excellent structural properties at elevated temperatures [11, 12]. From a more fundamental perspective, these materials also exhibit a range of interesting physical behaviours. For example, various HEAs and related medium-entropy systems have previously been shown to exhibit superconductivity [13], complex magnetism [14], quantum critical behaviour [15] and high levels of Fermi surface smearing [16].

One composition of particular interest is the well-studied, equiatomic AlTiVCr HEA, which has a low density compared to many other bcc HEAs (because it contains only Al and early-3d transition metals) but also retains good mechanical properties [17–20]. In contrast to many HEAs containing only transition metal elements and forming disordered solid solutions, the addition of

Al to HEAs is understood to promote atomic short- and long-range ordering tendencies [21, 22]. In the case of AlTiVCr, it is understood that the material undergoes a phase transition from an A2 (disordered bcc) phase to an ordered B2 (CsCl) phase which subsequently remains stable across a wide temperature range [20]. (The B2 structure, conceptually illustrated in Fig. 1, is a chemically ordered structure imposed on the bcc lattice.) AlTiVCr is therefore perhaps best referred to as a refractory high-entropy superalloy (RSA), on account of the analogy with Ni-Al superalloys which also form ordered intermetallic phases with exceptional mechanical properties [23].

Computational studies have a key role to play in elucidating the nature of atomic short- and long-range order in HEAs, and can also provide key insights into how the atomic-scale structure of these complex materials influences their physical properties [24–27]. The materials modeller’s ‘toolkit’ for studying the phase stability of HEAs includes: simulation approaches based on density functional theory (DFT) calculations [28–30]; interatomic potentials including both semi-empirical and machine-learning models [31–35]; and lattice-based models such as cluster expansions [36–39]. Specific to the study of alloy thermodynamics, a range of conventional and enhanced sampling techniques (*i.e.* Monte Carlo and related methods) can be used to study phase transitions and phase equilibria [24–27], as can semi-empirical thermodynamic approaches such as CALPHAD [40, 41]. There are also approaches available based on effective medium theories such as the coherent potential approximation (CPA) [42–44].

In this work, we present computational results which give detailed insight into the atomic-scale structure and

\* christopher.woodgate@bristol.ac.uk

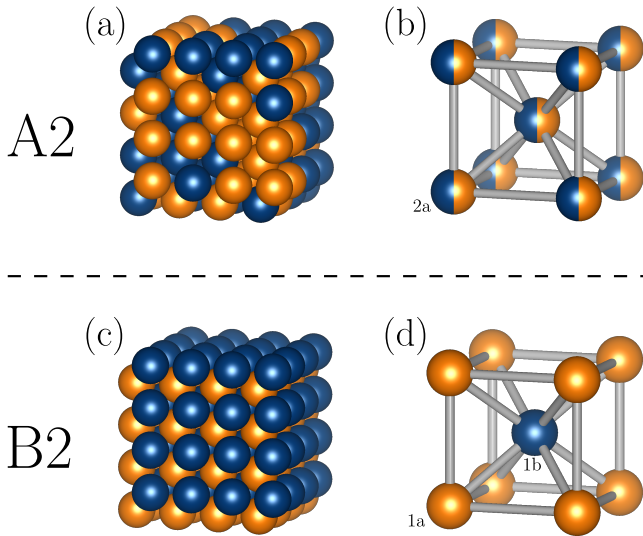


FIG. 1. Illustrations—for an equiatomic binary alloy—of the disordered bcc structure, Strukturbericht designation A2, and the ordered CsCl structure, Strukturbericht designation B2. Panel (a) shows a supercell representation of the A2 structure, while panel (b) shows a representation of the unit cell where half-coloured spheres indicate partial lattice site occupancies. Panel (c) then shows a supercell representation of the B2 structure, while panel (d) shows a representation of the unit cell. Such chemically-ordered structures can emerge in an alloy if it is annealed below its disorder-order transition temperature. In panels (b) and (d), lattice sites are given their Wyckoff labels. Images generated using VESTA [45].

physical properties of the AlTiVCr HEA. Specifically, we describe the alloy’s electronic structure, phase stability, and electronic transport properties using a combination of first-principles DFT calculations, a perturbative concentration wave analysis [46–48], and atomistic Monte Carlo simulations using a recovered pairwise form of the alloy’s internal energy. We also examine the electronic transport properties of the material, inspecting how chemical ordering affects this key physical property. In alignment with the available experimental data, as well as with previous computational studies, we predict a B2 chemical ordering emerging in the alloy at high temperatures, where Al and Ti move to separate sublattices while V and Cr express much weaker sublattice preferences. Counter-intuitively, this (partial) chemical ordering is found to result in an increased predicted residual resistivity for the alloy, a result attributed to a reduction in the electronic density of states at the Fermi level induced by the chemical ordering. Our atomistic Monte Carlo simulations then predict eventual ordering (at comparatively low temperatures) into a fully-ordered single-phase ground state accompanied, naturally, by a vanishing residual resistivity.

The remainder of this paper is structured as follows. First, in Sec. II, we outline our computationally efficient, multi-stage modelling approach for simulating the elec-

tronic structure, phase stability, and physical properties of HEAs. Subsequently, in Sec. III we present our results for the AlTiVCr HEA on which this work focuses, where our workflow predicts the aforementioned B2 chemical ordering emerging at high temperatures. We also elucidate the underlying physical mechanisms driving this chemical ordering and governing the material’s transport properties. This is achieved by describing the details of the alloy’s electronic structure in both disordered and ordered phases as modelled within the tenets of DFT. Finally, in Sec. IV, we summarise our results, draw relevant conclusions, and give an outlook on potential future avenues of study.

## II. METHODS

### A. Alloy thermodynamics and phase stability

#### 1. Electronic structure of the solid solution: The coherent potential approximation (CPA)

In this work, all electronic structure calculations are performed using the Korringa–Kohn–Rostoker (KKR) [49–51] formulation of DFT [52–54], which uses multiple-scattering theory [55] to construct the Green’s function for the Kohn–Sham equations. By virtue of the KKR method’s formulation in terms of scattering of electronic waves from an array of atomic lattice sites (scattering centres), in the context of disordered media such as alloys it is possible to develop effective medium theories for such media. These theories aim to construct configurationally-averaged Green’s functions representing the averaged electronic scattering properties of a given disordered medium, such as a substitutionally disordered alloy [56]. The most widely-used effective medium theory within the KKR method is the CPA [51, 55]. First introduced by Soven [57] in the context of scattering from Dirac  $\delta$ -function potentials in a 1D lattice, the CPA was subsequently generalised to three dimensions and potentials of finite spatial extent [58–60], as is required for use in the context of DFT calculations. The CPA has previously been utilised—with success—to model a wide range of HEA compositions and to study a variety of physical phenomena. Previous studies have shown that the CPA accurately captures details of HEAs’ electronic structure [16, 61] and magnetism [14, 62], as well as a range of transport [63–65] and structural [66–68] properties. We are therefore confident of its suitability for studying the AlTiVCr HEA in the present work.

#### 2. Energetic cost of atomic-scale chemical fluctuations: a concentration wave analysis

To study the phase stability of a particular alloy composition, it is necessary to consider how atoms of different chemical species are arranged on the underlying crystal

lattice, which is bcc in the context of the present work. In brief, an arrangement of atoms (a ‘configuration’) on a crystal lattice with lattice positions  $\{\mathbf{R}_i\}$  is specified by a set of *site-occupation numbers*,  $\{\xi_{i\alpha}\}$ , where  $\xi_{i\alpha} = 1$  if site  $i$  is occupied by an atom of chemical species  $\alpha$ , and  $\xi_{i\alpha} = 0$  otherwise. It is then natural to consider the average value of these site-occupation numbers, leading to the definition of the site-wise concentrations,

$$c_{i\alpha} := \langle \xi_{i\alpha} \rangle, \quad (1)$$

where  $\langle \cdot \rangle$  denotes an average taken with respect to the relevant thermodynamic ensemble. These site-wise concentrations represent atomic long-range order (ALRO) parameters classifying potential chemically ordered phases.

In the limit of high-temperature, where the free energy landscape is dominated by entropy, the alloy is fully disordered and the site-wise concentrations are spatially homogeneous, *i.e.* any atom can occupy any lattice site with probability equal to its average concentration in the alloy, denoted  $c_\alpha$ . This disordered state is typically referred to as a *solid solution*. With decreasing temperature, however, chemical order can emerge. The (now inhomogeneous) site-wise concentrations associated with a given chemical ordering can be written as a fluctuation about the homogeneous high-temperature reference state in a real-space representation as  $c_{i\alpha} = c_\alpha + \Delta c_{i\alpha}$ . Alternatively, the inhomogeneous state can be described in reciprocal-space using the language of *concentration waves* [69, 70] via

$$c_{i\alpha} = c_\alpha + \sum_{\mathbf{k}} e^{i\mathbf{k}\cdot\mathbf{R}_i} \Delta c_\alpha(\mathbf{k}), \quad (2)$$

where  $\Delta c_\alpha(\mathbf{k})$  represents a static concentration wave with wavevector  $\mathbf{k}$  and chemical polarisation  $\Delta c_\alpha$ . A conceptual illustration of a concentration wave modulating partial lattice site occupancies in a one-dimensional ‘alloy’ is given in Fig. 2. In three dimensions, for most chemical orderings, the sum over  $\mathbf{k}$  in Eq. (2) typically runs over a handful of high-symmetry  $\mathbf{k}$ -vectors. For example, the B2 structure shown in Fig. 1 is described by a concentration wave with wave vector  $\mathbf{k} = (0, 0, 2\pi/a)$  and equivalent [69].

The internal energy of the homogeneous, disordered alloy (*i.e.*  $E_{\text{CPA}}(\{c_{i\alpha}\})$  for  $c_{i\alpha} \equiv c_\alpha$ ) can be evaluated within the CPA [71, 72]. However, to assess the (free) energetic cost of atomic-scale chemical fluctuations represented by a given concentration wave it is necessary to consider how this quantity changes as the site-wise concentrations vary. To this end, concentration derivatives of  $E_{\text{CPA}}(\{c_{i\alpha}\})$  need be considered. To lowest-order, the relevant quantity is the second concentration derivative of the internal energy [46], denoted  $S_{i\alpha;j\alpha'}^{(2)}$  and defined as

$$S_{i\alpha;j\alpha'}^{(2)} \equiv \frac{\partial^2 E_{\text{CPA}}}{\partial c_{i\alpha} \partial c_{j\alpha'}} \Big|_{\{c_\alpha\}}. \quad (3)$$

Due to the translational symmetry of the underlying crystal, it is most convenient to evaluate the lattice Fourier

transform of this quantity,  $S_{\alpha\alpha'}^{(2)}(\mathbf{k})$ . The coupled set of equations which must be evaluated to obtain this quantity, including fully the rearrangement of charge due to chemical fluctuations, are given in Ref. 46, and we omit discussion of the details here for brevity. We emphasise here, though, that the alloy  $S^{(2)}$  theory [46–48]—which is a multicomponent generalisation of an earlier theory developed solely for binary alloys [73–75]—has previously been applied, with success, to the thermodynamics and phase stability of various Al-containing [76, 77], Ti-containing [77, 78], and refractory HEAs [78, 79]. We are therefore confident of its reliability in the context of the present work.

Proceeding, the change in free energy,  $\Delta\Omega$ , induced by a given (set of) concentration wave(s) modulating the site occupancies of the solid solution is then given by

$$\Delta\Omega = \frac{1}{2} \sum_{\mathbf{k}} \sum_{\alpha, \alpha'} \Delta c_\alpha(\mathbf{k}) [\beta^{-1} C_{\alpha\alpha'}^{-1} - S_{\alpha\alpha'}^{(2)}(\mathbf{k})] \Delta c_{\alpha'}(\mathbf{k}), \quad (4)$$

where  $\beta = \frac{1}{k_B T}$ , and  $C_{\alpha\alpha'}^{-1} = \frac{\delta_{\alpha\alpha'}}{c_\alpha}$  is associated with entropic contributions to the free energy. The matrix in

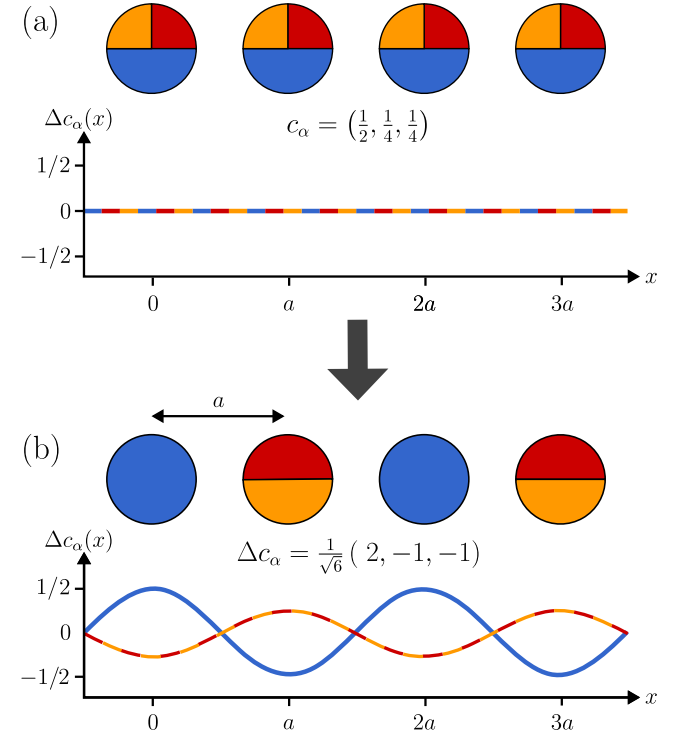


FIG. 2. Schematic illustration of a particular *concentration wave* modulating partial atomic lattice site occupancies in a toy, one-dimensional  $A_2BC$  alloy. In order, the chemical species are coloured blue, orange, and red. The first state of the alloy, shown in panel (a), is homogeneous, with all lattice site occupancies equal. The second state of the alloy, shown in panel (b), is obtained by modulating the occupancies of panel (a) with a concentration wave of wave vector  $\mathbf{k} = \frac{\pi}{a}$  and (normalised) chemical polarisation  $\Delta c_\alpha = \frac{1}{\sqrt{6}}(2, -1, -1)$ .

square brackets,  $[\beta^{-1}C_{\alpha\alpha'}^{-1} - S_{\alpha\alpha'}^{(2)}(\mathbf{k})]$ , we refer to as the *chemical stability matrix*. At high-temperatures its eigenvalues are strictly positive for all wavevectors, indicating that the solid solution is thermodynamically stable. However, with decreasing temperature some eigenvalue is anticipated to pass through zero at a given temperature,  $T_{\text{ord}}$ , for a given wave vector,  $\mathbf{k}_{\text{ord}}$ , and an ordering is inferred [46]. The eigenvector associated with the eigenvalue passing through zero then describes which chemical species partition themselves onto which sublattice(s) [46–48]. This analysis constitutes a mean-field, Landau-type theory for alloy phase stability, and is naturally anticipated to marginally overestimate the true chemical ordering temperature.

### 3. Recovery of atom-atom effective pair interactions

Going beyond the above Landau-type mean-field theory, the quantity  $S_{i\alpha;j\alpha'}^{(2)}$  can be related to a pairwise form of the alloy internal energy [46–48] which we refer to as the Bragg–Williams model [80, 81]. The Hamiltonian for this model takes the form

$$H(\{\xi_{i\alpha}\}) = \frac{1}{2} \sum_{i\alpha;j\alpha'} V_{i\alpha;j\alpha'} \xi_{i\alpha} \xi_{j\alpha'}, \quad (5)$$

where  $V_{i\alpha;j\alpha'} = -S_{i\alpha;j\alpha'}^{(2)}$  denotes the atom-atom *effective pair interaction* (EPI) between an atom of chemical species  $\alpha$  on lattice site  $i$  and an atom of chemical species  $\alpha'$  on lattice site  $j$ . As the underlying CPA reference medium is—on the average—spatially homogeneous and isotropic, so too are the atom-atom EPIs. We therefore write  $V_{\alpha,\alpha'}^{(n)}$  to denote the interaction between chemical species  $\alpha$  and  $\alpha'$  on coordination shell  $n$ , *i.e.* at  $n^{\text{th}}$ -nearest neighbour distance. Additionally, the EPIs are typically short-ranged and can be set to zero beyond some finite ‘cutoff’ distance, which further simplifies evaluation of Eq. (5) in practical calculations.

### 4. Atomistic Monte Carlo simulations

Using the Hamiltonian of Eq. (5), lattice-based Monte Carlo simulations can be used to investigate the phase behaviour of an alloy system in detail. In this work, two Monte Carlo schemes are used: the Metropolis–Hastings method [82, 83] and Wang–Landau sampling [83, 84]. Metropolis–Kawasaki dynamics [85], meaning that Monte Carlo moves consist of pairs of atoms being exchanged within the simulation cell, are used throughout. This ensures that the overall alloy composition remains fixed throughout a simulation.

In the Metropolis–Hastings algorithm [82, 83], trial moves from an initial configuration, labelled  $n$ , to a proposed candidate configuration, labelled  $m$ , are accepted

with probability

$$P_{n \rightarrow m} = \begin{cases} \exp(-\Delta E/k_B T), & \Delta E > 0, \\ 1, & \Delta E \leq 0, \end{cases} \quad (6)$$

where  $\Delta E = E_m - E_n$  is the corresponding change in internal energy,  $k_B$  is the usual Boltzmann constant, and  $T$  is the simulation temperature. In this work, the Metropolis–Hastings algorithm is primarily employed to generate equilibrated configurations at chosen temperatures for visualisation. Simulations begin from a randomly-generated supercell matching the target species concentrations, after which Monte Carlo sampling is carried out at the desired temperature. After a specified number of Monte Carlo steps, the system reaches an approximately equilibrated configuration suitable for visualisation and further analysis.

In contrast to the Metropolis–Hastings method, the Wang–Landau sampling algorithm [83, 84] is a flat-histogram scheme that enables direct determination of the density of states (DOS),  $g(E)$ , of any model with a Hamiltonian that defines the internal energy as a function of the model configuration. Because the DOS does not depend on temperature, once obtained it enables the computation of thermodynamic properties at arbitrary temperatures. Determination of the DOS is achieved by grouping the spectrum of energies available to the system into distinct macrostates and constructing a histogram of energies representative of the true system DOS. An initial guess of the DOS (*e.g.*  $g(E) \equiv 1$ ) is iteratively refined over the course of a simulation run until convergence is achieved. A detailed discussion of this procedure in the context of simulation of alloys can be found in other works [77, 86], so we omit those details here.

With the DOS available following convergence of a Wang–Landau sampling run, the probability of observing a given energy  $E_j$  at temperature  $T$  is determined via

$$P(E_j, T) = \frac{g(E_j) e^{-E_j/k_B T}}{Z}, \quad (7)$$

where  $E_j$  labels an energy (macrostate) of the Wang–Landau histogram, and  $Z$  is the usual partition function. Knowledge of this probability distribution provides access to a range of thermodynamic observables. An example is the temperature-dependent specific heat,  $C_V$ , which is computed via [83]

$$C_V(T) = \frac{\langle E^2 \rangle - \langle E \rangle^2}{k_B T^2}, \quad (8)$$

where the required ensemble averages,  $\langle \cdot \rangle$ , are evaluated using the probability distribution of Eq. (7).

To quantify atomic short-range order in a simulation, the multicomponent Warren–Cowley atomic short-range order (ASRO) parameters [87, 88],  $\alpha_n^{pq}$  are used. These are defined as

$$\alpha_n^{pq} = 1 - \frac{P_n^{pq}}{c_q}, \quad (9)$$

where  $P_n^{pq}$  is the conditional probability of finding a pair of atoms of chemical species  $p$  and chemical species  $q$  on coordination shell  $n$ , and  $c_q$  is the overall concentration of element  $q$ . Positive  $\alpha_n^{pq}$  values indicate that  $p$ - $q$  pairs occur less frequently than in a fully random alloy, negative values instead signal a preference for such pairings, and  $\alpha_n^{pq} = 0$  corresponds to complete disorder.

These ASRO parameters are first evaluated as functions of energy across the Wang–Landau-sampled range (via averages over the configurations in each energy bin) and are then converted into temperature-dependent quantities using a weighted sum over the energies [77], where the weights are simply the probabilities of Eq. (7). Though these ASRO parameters are incomplete [89], *i.e.* they do not capture all details of all possible local chemical environments, we consider them sufficient for the purposes of the present study.

### B. Electronic transport properties

Given its construction as a scattering theory for electronic waves, it is perhaps unsurprising that the KKR-CPA is well-suited to the study of the electronic transport properties of disordered systems [90]. In this work, we focus solely on the residual resistivity, an intrinsic physical quantity which is finite for a disordered (or partially ordered) alloy in which translational symmetry is broken and Bloch states are not eigenstates of the Hamiltonian.

From the configurationally-averaged Green's function,  $G$ , obtained using the KKR-CPA, the Kubo–Greenwood formula [91, 92] can be applied and the residual resistivity calculated according to [64, 77, 90]

$$\sigma_{\mu\nu} = \frac{\hbar}{\pi V} \text{Tr} \langle j_\mu \text{Im}G^+(E_F) j_\nu \text{Im}G^+(E_F) \rangle_{\text{CPA}}, \quad (10)$$

where  $V$  is the simulation cell volume;  $G^+(E_F)$  is the retarded Green's function at the Fermi level,  $E_F$ ; and  $j_\mu$  is the current density operator with Cartesian coordinate indices  $\mu$  and  $\nu$ . Angled brackets,  $\langle \cdot \rangle_{\text{CPA}}$ , are used to indicate the CPA average over substitutional disorder. From the conductivity tensor, the residual resistivity of a material is recovered as a simple post-processing step.

### C. Computational details

All self-consistent KKR-CPA calculations were performed within the atomic sphere approximation (ASA) [93] using the all-electron SPR-KKR package [51, 94]. Throughout, the lattice parameter of the system was fixed to the experimental value of 3.075 Å [17]. The local density approximation (LDA) was utilised throughout, specifically the parametrisation of Vosko, Wilks, and Nusair [95]. For self-consistent calculations, Brillouin zone integrations were performed using an SPR-KKR parameter setting of `NKTAB=5000`, which results in a  $62 \times 62 \times 62$   $\mathbf{k}$ -point mesh over the

first Brillouin zone in the case of the disordered bcc (A2) structure. A 32-point semi-circular contour in the complex plane was used for energy integrations during self-consistent calculations. Transport calculations were performed using the Kubo–Greenwood formalism as implemented in SPR-KKR, with Brillouin-zone integrations performed using a parameter of `NKTAB=150,000`, resulting in a dense  $53 \times 53 \times 53$   $\mathbf{k}$ -point mesh over the first Brillouin zone of the B2 crystal structure. In the case of initial self-consistent calculations and the concentration wave analysis, scalar-relativistic calculations were used, while for the transport analysis fully-relativistic calculations were utilised.

The concentration wave analysis was performed using an in-house implementation of the  $S^{(2)}$  theory for multicomponent alloys, the computational details of which have been discussed in earlier works [46–48]. (This code includes an adaptive meshing scheme for efficient Brillouin zone integrations [96].) The quantity  $S_{\alpha\alpha'}^{(2)}(\mathbf{k})$  was sampled at a total of 56  $\mathbf{k}$ -points in the irreducible Brillouin zone, including high-symmetry points. From an initial analysis of atom-atom EPIs,  $V_{\alpha\alpha'}^{(n)}$ , fitted to the first 10 coordination shells of the bcc lattice, it was determined that a fit to the first 6 coordination shells of the bcc lattice, corresponding to a real-space ‘cutoff’ of 6.15 Å, was deemed sufficient to capture the reciprocal-space  $S_{\alpha\alpha'}^{(2)}(\mathbf{k})$  data with good accuracy.

All fixed-lattice Monte Carlo simulations (Metropolis–Hastings and Wang–Landau) were performed using the BRAWL package [97], with details of the employed parallelisation and parallel load-balancing schemes for the Wang–Landau sampling algorithm as discussed in Ref. [86]. The final Wang–Landau sampling run utilised a simulation supercell consisting of  $10 \times 10 \times 10$  bcc cubic unit cells for a total of 2000 atoms. The total energy range for the 2000-atom simulation cell of  $-65$  eV/atom to  $10$  eV/atom was divided into 1024 energy sub-domains. (For tests of convergence of key quantities such as the specific heat with respect to the size of simulation cell, the energy range and numbers of energy bins were scaled appropriately.) The applied Wang–Landau flatness tolerance, used to determine convergence of the energy histogram at a given iteration, was set to be  $F > 0.8$ . The Wang–Landau update factor tolerance  $\log f$ , was set to be  $1 \cdot 10^{-12}$  for all simulation runs.

## III. RESULTS AND DISCUSSION

### A. Electronic structure of the A2 phase

We begin by describing the electronic structure of the AlTiVCr HEA in its disordered bcc (A2) phase. In the context of this particular alloy, it is important to treat magnetism appropriately; not only has AlTiVCr previously been proposed as a candidate ‘spin filter’ material [98–101], but—more generally—magnetism can of

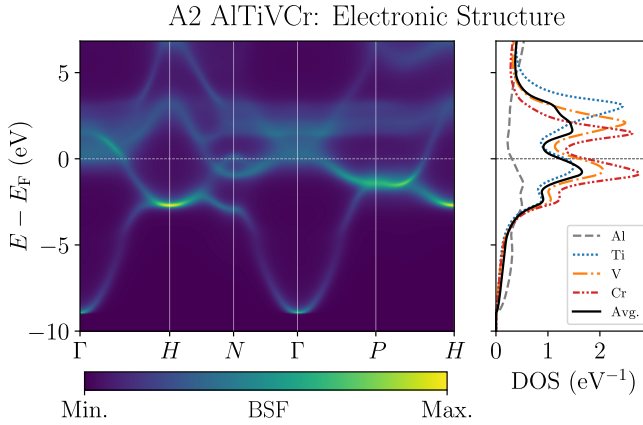


FIG. 3. Bloch spectral function (a ‘bandstructure’ for the disordered alloy) and species-resolved electronic DOS around the Fermi energy,  $E_F$  for the AlTiVCr high-entropy alloy as described within the KKR-CPA for the A2 (disordered bcc) phase. A degree of hybridisation between the  $sp$ -like states of Al and the  $3d$  states of the transition metals is indicated by the localised peaks/troughs in the species-resolved DOS for Al at energies where there are peaks/troughs in the DOS associated with the narrow  $3d$  bands of the transition metals.

ten play a key role in determining the free energy landscape of alloys [102–104]. In this work, where all calculations are performed at the experimental lattice constant, we consistently find that elemental magnetic moments are quenched, *i.e.* they collapse to zero during the self-consistency cycle. This is consistent with the supercell calculations of Ref. 30, where (for a range of DFT exchange-correlation functionals) elemental magnetic moments were only reliably obtained when an expanded lattice parameter was employed. We therefore conclude that the appropriate magnetic state for our purposes is non-magnetic.

Shown in Fig. 3 are plots of the Bloch spectral function (BSF) along high-symmetry lines of the irreducible Brillouin zone (IBZ) of the bcc lattice, as well as plots of the averaged and species-resolved electronic DOS around the Fermi level for disordered bcc (A2) AlTiVCr. It can be seen that the band structure of the material is heavily smeared by the chemical disorder—a consequence of the broken translational symmetry. We associate the dispersive, near-parabolic bands seen in the BSF plot with the  $sp$ -states of both Al and the transition metals, while the comparatively narrow bands around the Fermi level are associated with the  $3d$  bands of Ti, V, and Cr. Related to the increasing valence numbers of the elements, it can be seen that—integrated up to the Fermi level—the area under the electronic DOS curve is smallest for Al, then increases for Ti, then V, through to Cr, for which it is largest. Finally, we note that a degree of hybridisation between the  $sp$ -like states of Al and the  $3d$  states of the transition metals can be seen. The hallmark of this is the presence of localised peaks/troughs in the species-resolved DOS for Al which are aligned with localised

peaks/troughs in the same curves for the transition metals.

## B. Concentration wave analysis

Proceeding, we perform a concentration wave analysis to garner information about the dominant atom-atom correlations and infer which chemical ordering(s) are likely to emerge as the alloy is cooled. Shown in Fig. 4 are plots of (a)  $S_{\alpha\alpha'}^{(2)}(\mathbf{k})$  and (b) the eigenvalues of the chemical stability matrix of Eq. (4), the latter of which is evaluated at a temperature of  $T = 1800$  K. For both, these data are plotted along selected high-symmetry lines of the IBZ.

We consider first the raw  $S_{\alpha\alpha'}^{(2)}(\mathbf{k})$  data, shown in panel (a) of Fig. 4. When the quantity  $S_{\alpha\alpha'}^{(2)}(\mathbf{k})$  takes large values and varies strongly as a function of  $\mathbf{k}$ , it indicates that a pair of elements interacts strongly, while when this quantity takes small values and varies weakly it indicates that a pair of elements interacts weakly. It can be seen that, in this case, the strongest atomic interactions are between Al-Al, Al-Ti, and Ti-Ti pairs, with other el-

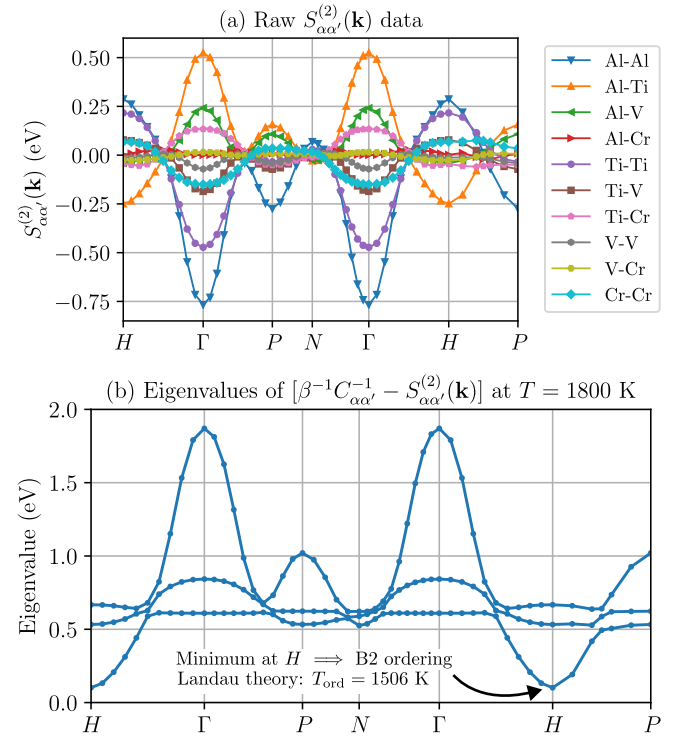


FIG. 4. Plots of data associated with the concentration wave analysis performed using the alloy  $S^{(2)}$  theory [46–48]. Panel (a) shows the raw  $S_{\alpha\alpha'}^{(2)}(\mathbf{k})$  data plotted along selected high-symmetry lines of the IBZ of the bcc lattice, while panel (b) shows the eigenvalues of the chemical stability matrix along those same high-symmetry directions. That the minimum eigenvalue lies at  $H$  in panel (b) indicates that a B2 chemical ordering is favoured.

TABLE I. Sublattice partial occupancies for the B2 structure predicted by the concentration wave analysis. The strongest site preferences are for Al and Ti, while V and Cr remain spread more evenly across both sublattices.

Lattice site	$c_{\text{Al}}$	$c_{\text{Ti}}$	$c_{\text{V}}$	$c_{\text{Cr}}$
1a	0.500	0.027	0.197	0.276
1b	0.000	0.473	0.303	0.224

ements interacting more weakly. This is consistent with the strong propensity for Al-Ti alloys to form ordered intermetallic compounds [105].

Next, we consider the eigenvalues of the chemical stability matrix, shown in panel (b) of Fig. 4. Here, the lowest-lying eigenvalue is most relevant, as this indicates the dominant chemical order [47]. A minimum at the  $H$  point, corresponding to  $\mathbf{k} = (0, 0, 2\pi/a)$  describes a B2 chemical ordering [69, 79]. The associated (normalised) eigenvector is  $\Delta c_\alpha = (0.734, -0.656, -0.156, 0.078)$ , while the predicted ordering temperature (the temperature at which this eigenvalue passes through zero) is  $T_{\text{ord}} = 1506$  K. The eigenvector indicates that Al moves strongly to one sublattice and Ti strongly the other. The smaller  $\Delta c_\alpha$  values associated with V and Cr indicate a weak preference for V moving to the Ti sublattice and Cr the Al sublattice. If the amplitude of this predicted concentration wave is allowed to ‘grow’ until one sublattice contains (at least) one atomic species whose concentration reaches zero, we obtain a partially-ordered B2 structure whose (partial) site occupancies are provided in Table I. A self-consistent KKR-CPA calculation performed on this B2 (partially) ordered structure reveals that it is 53 meV/atom lower in energy than the disordered A2 structure.

These data are broadly in alignment with several previous studies. For example, Huang *et al.* [20] used CALPHAD to predict a B2 ordering temperature for the equiatomic composition of 1239 K. A separate study by Widom [30] used first-principles calculations (PBE exchange-correlation functional) to predict a B2 ordering temperature of 1200 K, which was characterised by Al moving to one sublattice, Ti to the other, and with Cr and V expressing marginally weaker sublattice preferences, in excellent alignment with our own data. Experimentally, it is widely reported that this alloy forms a B2 phase across a wide temperature range [17], which is in agreement with our own results. However, it should be noted that the nature of our predicted B2 chemical ordering differs from that proposed by Stephen *et al.* [101], who suggested that Al and Ti would occupy one sublattice while Cr and V occupy the other. We stress, though, that no assessment of the thermodynamic stability of this proposed structure is provided by these authors.

From the reciprocal-space  $S_{\alpha\alpha'}^{(2)}(\mathbf{k})$  data, we subsequently recover atom-atom EPIs,  $V_{\alpha,\alpha'}^{(n)}$ , suitable for use in atomistic simulations. EPIs for the AlTiVCr sys-

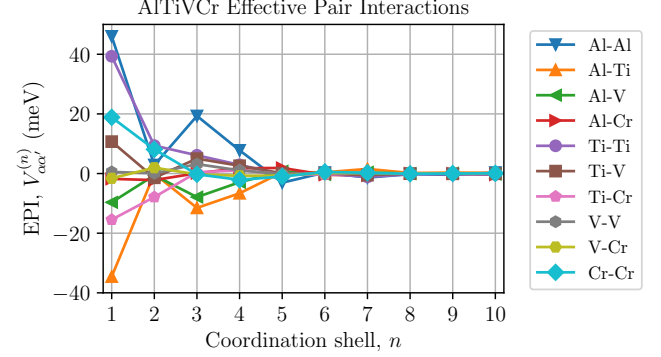


FIG. 5. Calculated real-space atom-atom effective pair interactions for the AlTiVCr high-entropy alloy recovered from the *ab initio* concentration wave analysis. A negative value of  $V_{\alpha,\alpha'}^{(n)}$  indicates that it is energetically favourable to find the pair  $\alpha-\alpha'$  on coordination shell  $n$ , while a positive value of  $V_{\alpha,\alpha'}^{(n)}$  indicates the opposite. It can be seen that the strongest interactions are between Al-Al, Al-Ti, and Ti-Ti pairs, and also that interactions tail off quickly with increasing distance.

tem for the first ten coordination shells of the bcc lattice are shown in Fig. 5. Consistent with the discussion above, here it is seen that the strongest EPIs are for Al-Al, Al-Ti and Ti-Ti pairs, which is most evident at nearest-neighbour distance, *i.e.* for  $n = 1$ . It can also be seen that the interactions are relatively short-ranged, which justifies our truncation of interactions beyond sixth-nearest neighbour distance in the fixed-lattice Monte Carlo simulations which are to follow.

### C. Atomistic, fixed-lattice Monte Carlo simulations

Using the recovered atom-atom EPIs graphed in Fig. 5, we subsequently perform fixed-lattice Monte Carlo simulations to examine the phase behaviour of the alloy in detail. This serves both to validate the mean-field Landau theory, as well as to allow us to examine any additional phase transitions occurring at temperatures below the initial ordering temperature. Fig. 6 shows plots of the temperature-dependent Warren-Cowley ASRO parameters and simulation specific heat as obtained using Wang-Landau sampling, while Fig. 7 shows representative equilibrium atomic configurations at selected temperatures obtained using Metropolis–Hastings Monte Carlo. Convergence of simulation quantities with respect to system size was tested by performing simulations on a range of system sizes from  $N = 16$  atoms ( $2 \times 2 \times 2$  cubic bcc unit cells) to  $N = 2000$  atoms ( $10 \times 10 \times 10$  cubic bcc unit cells). Results for convergence of the specific heat with respect to system size are shown in panel (c) of Fig. 6. The minimal changes in specific heat data between the cases  $N = 1024$  and  $N = 2000$  confirm that our simulation results are well-converged with respect to this key simulation variable.

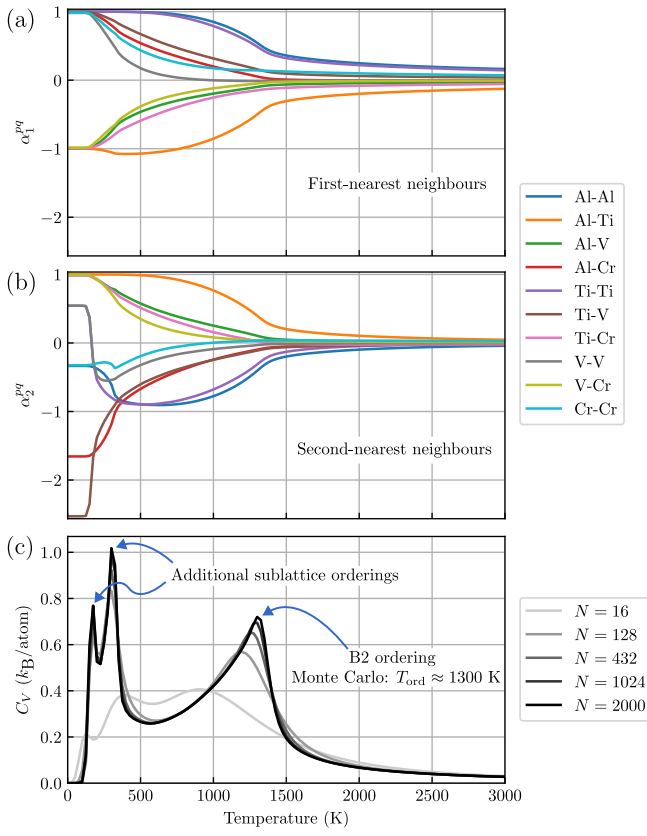


FIG. 6. Plots of the Warren-Cowley ASRO parameters on the first (a) and second (b) coordination shells of the bcc lattice, together with (c) the specific heat as a function of temperature obtained using fixed-lattice Monte Carlo simulations. The data in panels (a) and (b) were obtained for a Wang-Landau sampling simulation on a system containing  $N = 2000$  atoms, while panel (c) evidences the convergence of results with respect to system size. The high-temperature peak in the specific heat data is associated with the initial B2 chemical ordering, while the low temperature peaks are associated with additional sublattice ordering into an ordered single-phase ground state, shown in panel (a) of Fig. 7.

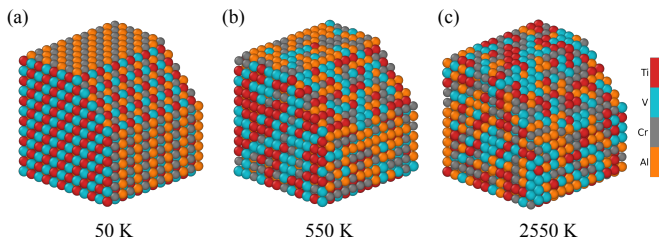


FIG. 7. Representative equilibrium configurations for the Al-TiVCr HEA at (a) 50 K, (b) 550 K, and (c) 2550 K. Al, Ti, V and Cr are coloured orange, red, turquoise and grey respectively. The progression from fully disordered bcc to partially-ordered B2 through to a fully-ordered, single-phase ground state with decreasing simulation temperature can clearly be seen. Images generated using OVITO [106].

Inspecting the ASRO and specific heat data shown in Fig. 6, three phase transitions can clearly be identified. At high temperature, AlTiVCr is in a fully disordered bcc (A2) structure, a sample configuration of which is shown in panel (c) of Fig. 7. As the alloy is cooled from this high-temperature state, a phase transition occurs at  $T_{\text{ord}} \approx 1300$  K—indicated by a peak in the specific heat—and AlTiVCr takes on the partially-ordered B2 (CsCl) structure, a sample configuration of which is shown in panel (b) of Fig. 7. (That the ordering temperature predicted by the Monte Carlo simulations is lower than that predicted by the earlier concentration wave analysis is consistent with the fact that the former includes rigorously local thermal fluctuations, while the latter represents a Landau-type mean-field theory.) In this B2 structure, Al and Ti atoms move to separate sublattices. This is evidenced by the negative (positive) value of  $\alpha_1^{pq}$  ( $\alpha_2^{pq}$ ) for Al-Ti pairs—indicating these pairs are favoured as nearest neighbours and disfavoured as second-nearest neighbours—and positive (negative) values of  $\alpha_1^{pq}$  ( $\alpha_2^{pq}$ ) for Al-Al and Ti-Ti pairs—indicating these pairings are disfavoured as nearest-neighbours and favoured as second-nearest neighbours. Weaker sublattice preferences for Cr and V can be seen, with Ti-Cr and Al-V pairs favoured as nearest-neighbours and disfavoured as second-nearest neighbours, while Al-Cr and Ti-V pairs are disfavoured as nearest neighbours and favoured as second-nearest neighbours. This indicates that Cr atoms preferentially sit on the Al sublattice and V atoms the Ti sublattice. This transition is therefore consistent with the mean-field analysis presented above in Sec. III B, albeit with a reduction in the predicted ordering temperature, as is to be expected.

Upon further cooling, two further phase transitions can be seen at  $T \approx 300$  K and  $T \approx 175$  K, indicating two further sublattice orderings. The ordering at higher temperature corresponds to a layering of Al and Cr atoms on their sublattice, while the ordering at lower temperature corresponds to a layering of Ti and V atoms on their sublattice. The final, single-phase ground state is shown in panel (a) of Fig. 7. The two sublattice orderings predicted by this model are not identical; on the Al/Cr sublattice some Al-Cr nearest-neighbours remain, while on the V/Ti sublattice Ti-V nearest neighbours are expelled. This ground-state structure is thus similar in pair-preferences, though not identical in structure, to the Heusler-like structure shown in Fig. 1(a) of Ref. [107], which those authors label the Y-I structure. We stress, however, that our atom-atom EPs of Eq. (5) are most reliable in the limit of high-temperature, and that results for predicted ground-state structures must be interpreted cautiously. Additionally, the low predicted temperatures of these sublattice orderings in our calculations suggests that they may be challenging to observe experimentally.

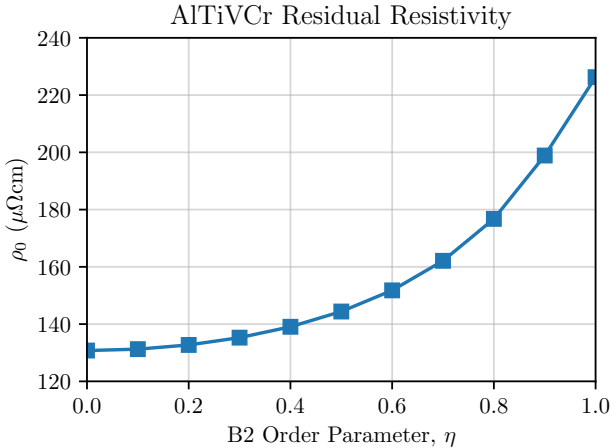


FIG. 8. Calculated residual resistivity of the AlTiVCr HEA as a function of B2 chemical order parameter,  $\eta$ . Counter-intuitively, the (partial) chemical ordering results in an increased predicted residual resistivity as compared to the fully disordered (A2) alloy. (The A2 phase corresponds to  $\eta = 0$ .)

#### D. Impact of the B2 chemical ordering on the alloy's electronic structure and transport properties

The study of the electronic transport properties of HEAs remains an active area of study [65], because the extreme compositional disorder in these complex systems results in heavily-smeared Fermi surfaces [16] and short electronic mean free paths [64]. Chemical orderings, such as the high-temperature B2 ordering predicted in this work for AlTiVCr, can substantially impact these transport properties due to the associated changes to the symmetries and electronic structure of the material [77].

Here, for the B2 ordering predicted by the *ab initio* concentration wave analysis, we assess the impact of this chemical ordering on the residual resistivity of the alloy within a Kubo-Greenwood linear-response framework. We define a B2 chemical order parameter  $\eta$  to quantify the degree of (partial) chemical ordering, where  $\eta = 0$  corresponds to the disordered solid solution, and  $\eta = 1$  corresponds to the largest permitted chemical fluctuation consistent with the predicted chemical polarisation  $\Delta c_\alpha(\mathbf{k} = (0, 0, 2\pi/a))$ . (This results in linear interpolation between the fully disordered state and the sublattice occupancies for the B2 structure provided in Table I.) Shown in Fig. 8 is a plot of the calculated residual resistivity,  $\rho_0$ , as a function of  $\eta$  for this system.

Two key observations should be made here. First is that, even compared to other HEAs [64, 65, 77], the calculated residual resistivity values are fairly large for Al-TiCrV for all values of  $\eta$ —this material is a ‘bad’ metal. Phenomenologically, we attribute this result to the differing nature of the electronic valence states associated with Al (a simple metal with no associated *d* electrons) as compared to the transition metals (all of which have 3*d*

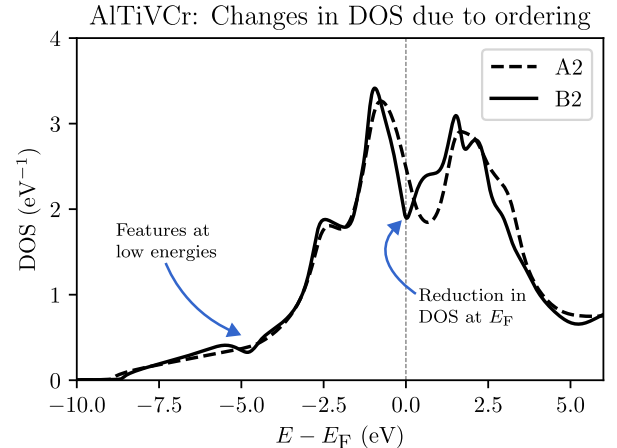


FIG. 9. Changes to the electronic DOS of the AlTiVCr HEA induced by the predicted B2 chemical ordering. Sharper features can be seen to emerge due to the ordering, along with a reduced DOS at the Fermi level.

states near the Fermi level) present in the composition, which results in strong electronic scattering. The strong electronic scattering caused by 3*d* solutes in Al-based binary alloys is discussed further by Samolyuk, Shyam, and Yoon [108], and we assert that similar scattering mechanisms are at play in this complex HEA. The second key observation to be made is that the calculated residual resistivity *increases* as the system transitions from the fully-disordered A2 structure to the (partially) ordered B2 structure. This result is perhaps unexpected—chemical ordering typically represents the restoration of (at least some level of) translational symmetry and thus is expected to result in a reduced resistivity. However, it is perhaps reminiscent of the so-called ‘komplex’ or *K*-state phenomenon, first observed in Ni-Cr alloys [109], where a degree of ASRO can increase the residual resistivity of an alloy [110].

To interpret this result, we look to changes in the electronic structure of the alloy as a result of the chemical ordering. Shown in Fig. 9 are plots of the total DOS for the alloy in both its disordered (A2) state and in our predicted B2 chemically-ordered structure. It can be seen that, compared to the A2 structure, the DOS for the B2 structure has some sharper features at low energies, indicative of the formation of bonding states, and a reduced value at the Fermi level. This shift of  $E_F$  into a DOS minimum can be described as a pseudogap-like depression [30], as widely discussed for Al-rich transition-metal intermetallics and attributed to electron diffraction at prominent Bragg planes of the reciprocal lattice together with strong Al(*sp*)-transition-metal(*d*) hybridization [111]. Since the DOS at the Fermi level dictates the number of available charge carriers, and thus is key in determining electronic transport properties. As the electronic structure remains heavily smeared by the residual chemical disorder in the predicted B2 structure, we de-

duce that the increased residual resistivity of the alloy as a result of the ordering has its origins primarily in the reduction of available states at the Fermi level induced by the ordering, similar to the mechanism discussed in Ref. [77].

#### IV. SUMMARY AND CONCLUSIONS

In summary, results have been presented analysing the electronic structure, phase stability, and physical properties of the lightweight AlTiVCr HEA. The methods used include self-consistent DFT calculations within the KKR-CPA, an *ab initio* concentration wave analysis, an electronic transport analysis using Kubo–Greenwood linear response theory, and fixed-lattice Monte Carlo simulations using both the Metropolis–Hastings and Wang–Landau sampling algorithms.

In alignment with existing experimental and computational data, a B2 chemical ordering was predicted to occur in the alloy at high temperatures. ( $T_{\text{ord}} \approx 1300$  K determined from fixed-lattice Monte Carlo simulations.) This ordering is driven primarily by Al and Ti moving to separate sublattices, with V and Cr expressing weaker site preferences. The influence of this chemical ordering on the electronic transport properties of the alloy were subsequently examined, and it was found that the chemical ordering resulted in an *increased* residual resistivity as compared to the disordered alloy, which is understood to originate primarily from a reduction in the electronic DOS at the Fermi level. Finally, in addition to the high-temperature B2 ordering, atomistic Monte Carlo simulations revealed the predicted low-temperature ground state of the alloy within this modelling approach to be a fully-ordered, single-phase ground state.

The main implications of this work are three-fold. First, these results provide detailed insight into the atomic-scale structure and physical properties of this well-studied HEA, aligning with existing experimental data, as well as computational studies performed using alternative modelling approaches. This therefore serves as an important validation study. Second, our residual resistivity calculations confirm that measurement of electronic transport properties could be a useful tool to detect chemical order in this and related alloy compositions. Third, the work serves as further evidence of the reliability of the KKR-CPA and associated analyses for studying disorder-order transitions in high-entropy alloys. Future work on the AlTiVCr HEA could seek to examine beyond-DFT methods, such as dynamical mean-field theory (DMFT) [112], to improve the description of electronic correlations and examine the apparently subtle magnetism of this complex material. Future work using the outlined concentration-wave-based modelling approach for assessing HEA phase stability could seek to perform high-throughput studies searching for new potential HEA compositions with desirable physical properties.

#### ACKNOWLEDGMENTS

C.D.W. thanks Prof. Julie B. Staunton (Department of Physics, University of Warwick, United Kingdom) for provision of the code implementing the  $S^{(2)}$  theory for multicomponent alloys as used in this work, and for helpful discussions. C.D.W. acknowledges support from a UK Engineering and Physical Sciences Research Council (EPSRC) Doctoral Prize Fellowship at the University of Bristol, Grant EP/W524414/1. H.J.N. is supported by a studentship within the EPSRC Centre for Doctoral Training in Modelling of Heterogeneous Systems, Grant EP/S022848/1. D.R. acknowledges financial support from the Deutsche Forschungsgemeinschaft (DFG) under Project No. 528706678 and from the project MEBIOSYS, funded under Project No. CZ.02.01.01/00/22.008/0004634 by the Johannes Amos Comenius Programme, call Excellent Research.

The authors also acknowledge the use of compute resources provided by the Isambard 3 high-performance computing (HPC) facility. Isambard 3 is hosted by the University of Bristol and operated by the GW4 Alliance (<https://gw4.ac.uk>) and is funded by UK Research and Innovation; and the EPSRC, Grant EP/X039137/1. Additional compute resources were provided by the Advanced Computing Research Centre (ACRC) of the University of Bristol, and by the Scientific Computing Research Technology Platform (SCRTP) of the University of Warwick.

#### AUTHOR CONTRIBUTIONS

C.D.W. conceived of the approach, with input from all authors. N.F.P. performed self-consistent SPR-KKR calculations for the disordered A2 phase under the supervision of D.R.. C.D.W. performed the concentration wave analysis and recovered the atom-atom effective pair interactions. H.J.N. implemented the Wang–Landau sampling algorithm in the BRAWL package and performed the fixed-lattice Monte Carlo simulations. N.F.P. performed self-consistent SPR-KKR calculations and electronic transport analysis for the predicted B2 ordered structures under the supervision of D.R.. C.D.W. prepared the first draft of the manuscript with input from H.J.N.. Subsequently, all authors revised the manuscript and approved its final version.

#### DATA AVAILABILITY

All data supporting the findings of this study are openly available at the following DOI/URL: <https://doi.org/10.5281/zenodo.18095932>. The all-electron SPR-KKR package, used for performing self-consistent KKR-CPA calculations and the electronic transport analysis, is available at <https://sprkkr.org>.

The BRAWL package, used for performing the fixed-lattice Monte Carlo simulations, is available at <https://github.com/ChrisWoodgate/BraWL>. The code

implementing the  $S^{(2)}$  theory for multicomponent alloys used in the concentration wave analysis is available from C.D.W. upon reasonable request.

---

[1] J.-W. Yeh, S.-K. Chen, S.-J. Lin, J.-Y. Gan, T.-S. Chin, T.-T. Shun, C.-H. Tsau, and S.-Y. Chang, Nanostructured High-Entropy Alloys with Multiple Principal Elements: Novel Alloy Design Concepts and Outcomes, *Advanced Engineering Materials* **6**, 299 (2004).

[2] B. Cantor, I. T. H. Chang, P. Knight, and A. J. B. Vincent, Microstructural development in equiatomic multicomponent alloys, *Materials Science and Engineering: A* **375-377**, 213 (2004).

[3] D. B. Miracle and O. N. Senkov, A critical review of high entropy alloys and related concepts, *Acta Materialia* **122**, 448 (2017).

[4] E. P. George, D. Raabe, and R. O. Ritchie, High-entropy alloys, *Nature Reviews Materials* **4**, 515 (2019).

[5] B. Gludovatz, A. Hohenwarter, D. Catoor, E. H. Chang, E. P. George, and R. O. Ritchie, A fracture-resistant high-entropy alloy for cryogenic applications, *Science* **345**, 1153 (2014).

[6] B. Gludovatz, A. Hohenwarter, K. V. S. Thurston, H. Bei, Z. Wu, E. P. George, and R. O. Ritchie, Exceptional damage-tolerance of a medium-entropy alloy CrCoNi at cryogenic temperatures, *Nature Communications* **7**, 10602 (2016).

[7] D. Liu, Q. Yu, S. Kabra, M. Jiang, P. Forna-Kreutzer, R. Zhang, M. Payne, F. Walsh, B. Gludovatz, M. Asta, A. M. Minor, E. P. George, and R. O. Ritchie, Exceptional fracture toughness of CrCoNi-based medium- and high-entropy alloys at 20 kelvin, *Science* **378**, 978 (2022).

[8] Y. Qiu, S. Thomas, M. A. Gibson, H. L. Fraser, and N. Birbilis, Corrosion of high entropy alloys, *npj Materials Degradation* **1**, 15 (2017).

[9] O. El-Atwani, N. Li, M. Li, A. Devaraj, J. K. S. Baldwin, M. M. Schneider, D. Sobieraj, J. S. Wróbel, D. Nguyen-Manh, S. A. Maloy, and E. Martinez, Outstanding radiation resistance of tungsten-based high-entropy alloys, *Science Advances* **5**, eaav2002 (2019).

[10] O. El Atwani, H. T. Vo, M. A. Tunes, C. Lee, A. Alvarado, N. Krienke, J. D. Poplawsky, A. A. Kohnert, J. Gigax, W.-Y. Chen, M. Li, Y. Q. Wang, J. S. Wróbel, D. Nguyen-Manh, J. K. S. Baldwin, O. U. Tukac, E. Aydogan, S. Fensin, and E. Martinez, A quinary WTaCrVHf nanocrystalline refractory high-entropy alloy withholding extreme irradiation environments, *Nature Communications* **14**, 2516 (2023).

[11] S. Praveen and H. S. Kim, High-Entropy Alloys: Potential Candidates for High-Temperature Applications – An Overview, *Advanced Engineering Materials* **20**, 1700645 (2018).

[12] J. Chen, X. Zhou, W. Wang, B. Liu, Y. Lv, W. Yang, D. Xu, and Y. Liu, A review on fundamental of high entropy alloys with promising high-temperature properties, *Journal of Alloys and Compounds* **760**, 15 (2018).

[13] P. Koželj, S. Vrtnik, A. Jelen, S. Jazbec, Z. Jagličić, S. Maiti, M. Feuerbacher, W. Steurer, and J. Dolinšek, Discovery of a Superconducting High-Entropy Alloy, *Physical Review Letters* **113**, 107001 (2014).

[14] D. Billington, A. D. N. James, E. I. Harris-Lee, D. A. Lagos, D. O'Neill, N. Tsuda, K. Toyoki, Y. Kotani, T. Nakamura, H. Bei, S. Mu, G. D. Samolyuk, G. M. Stocks, J. A. Duffy, J. W. Taylor, S. R. Giblin, and S. B. Dugdale, Bulk and element-specific magnetism of medium-entropy and high-entropy Cantor-Wu alloys, *Physical Review B* **102**, 174405 (2020).

[15] B. C. Sales, K. Jin, H. Bei, G. M. Stocks, G. D. Samolyuk, A. F. May, and M. A. McGuire, Quantum Critical Behavior in a Concentrated Ternary Solid Solution, *Scientific Reports* **6**, 26179 (2016).

[16] H. C. Robarts, T. E. Millichamp, D. A. Lagos, J. Laverock, D. Billington, J. A. Duffy, D. O'Neill, S. R. Giblin, J. W. Taylor, G. Kontrym-Sznajd, M. Samsel-Czekala, H. Bei, S. Mu, G. D. Samolyuk, G. M. Stocks, and S. B. Dugdale, Extreme Fermi Surface Smearing in a Maximally Disordered Concentrated Solid Solution, *Physical Review Letters* **124**, 046402 (2020).

[17] Y. Qiu, Y. Hu, A. Taylor, M. Styles, R. Marceau, A. Ceguerra, M. Gibson, Z. Liu, H. Fraser, and N. Birbilis, A lightweight single-phase AlTiVCr compositionally complex alloy, *Acta Materialia* **123**, 115 (2017).

[18] Y. Qiu, S. Thomas, M. Gibson, H. Fraser, K. Pohl, and N. Birbilis, Microstructure and corrosion properties of the low-density single-phase compositionally complex alloy AlTiVCr, *Corrosion Science* **133**, 386 (2018).

[19] X. Huang, J. Miao, and A. A. Luo, Lightweight Al-CrTiV high-entropy alloys with dual-phase microstructure via microalloying, *Journal of Materials Science* **54**, 2271 (2019).

[20] X. Huang, J. Miao, and A. A. Luo, Order-disorder transition and its mechanical effects in lightweight AlCrTiV high entropy alloys, *Scripta Materialia* **210**, 114462 (2022).

[21] O. Senkov, S. Senkova, and C. Woodward, Effect of aluminum on the microstructure and properties of two refractory high-entropy alloys, *Acta Materialia* **68**, 214 (2014).

[22] O. N. Senkov, C. Woodward, and D. B. Miracle, Microstructure and Properties of Aluminum-Containing Refractory High-Entropy Alloys, *JOM* **66**, 2030 (2014).

[23] D. B. Miracle, M.-H. Tsai, O. N. Senkov, V. Soni, and R. Banerjee, Refractory high entropy superalloys (RSAs), *Scripta Materialia* **187**, 445 (2020).

[24] M. Widom, Modeling the structure and thermodynamics of high-entropy alloys, *Journal of Materials Research* **33**, 2881 (2018).

[25] M. Eisenbach, Z. Pei, and X. Liu, First-principles study of order-disorder transitions in multicomponent solid-solution alloys, *Journal of Physics: Condensed Matter* **31**, 273002 (2019).

[26] A. Ferrari, B. Dutta, K. Gubaev, Y. Ikeda, P. Srinivasan, B. Grabowski, and F. Körmann, Frontiers in atomistic simulations of high entropy alloys, *Journal of Applied Physics* **128**, 150901 (2020).

[27] A. Ferrari, F. Körmann, M. Asta, and J. Neugebauer, Simulating short-range order in compositionally complex materials, *Nature Computational Science* **3**, 221 (2023).

[28] M. Widom, W. P. Huhn, S. Maiti, and W. Steurer, Hybrid Monte Carlo/Molecular Dynamics Simulation of a Refractory Metal High Entropy Alloy, *Metallurgical and Materials Transactions A* **45**, 196 (2014).

[29] A. Tamm, A. Aabloo, M. Klintenberg, M. Stocks, and A. Caro, Atomic-scale properties of Ni-based FCC ternary, and quaternary alloys, *Acta Materialia* **99**, 307 (2015).

[30] M. Widom, First-principles study of the order-disorder transition in the AlCrTiV high entropy alloy, *Physical Review Materials* **8**, 093603 (2024).

[31] T. Kostiuchenko, F. Körmann, J. Neugebauer, and A. Shapeev, Impact of lattice relaxations on phase transitions in a high-entropy alloy studied by machine-learning potentials, *npj Computational Materials* **5**, 55 (2019).

[32] C. W. Rosenbrock, K. Gubaev, A. V. Shapeev, L. B. Pártay, N. Bernstein, G. Csányi, and G. L. W. Hart, Machine-learned interatomic potentials for alloys and alloy phase diagrams, *npj Computational Materials* **7**, 24 (2021).

[33] F. Körmann, T. Kostiuchenko, A. Shapeev, and J. Neugebauer, B2 ordering in body-centered-cubic AlNbTiV refractory high-entropy alloys, *Physical Review Materials* **5**, 053803 (2021).

[34] Y.-W. Zhang, V. Sorkin, Z. H. Aitken, A. Politano, J. Behler, A. P. Thompson, T. W. Ko, S. P. Ong, O. Chalykh, D. Korogod, E. Podryabinkin, A. Shapeev, J. Li, Y. Mishin, Z. Pei, X. Liu, J. Kim, Y. Park, S. Hwang, S. Han, K. Sheriff, Y. Cao, and R. Freitas, Roadmap for the development of machine learning-based interatomic potentials, *Modelling and Simulation in Materials Science and Engineering* **33**, 023301 (2025).

[35] Y. Cao, K. Sheriff, and R. Freitas, Capturing short-range order in high-entropy alloys with machine learning potentials, *npj Computational Materials* **11**, 268 (2025).

[36] A. Fernández-Caballero, J. S. Wróbel, P. M. Mummery, and D. Nguyen-Manh, Short-Range Order in High Entropy Alloys: Theoretical Formulation and Application to Mo-Nb-Ta-V-W System, *Journal of Phase Equilibria and Diffusion* **38**, 391 (2017).

[37] D. Sobieraj, J. S. Wróbel, T. Rygier, K. J. Kurzydłowski, O. El Atwani, A. Devaraj, E. Martínez Saez, and D. Nguyen-Manh, Chemical short-range order in derivative Cr-Ta-Ti-V-W high entropy alloys from the first-principles thermodynamic study, *Physical Chemistry Chemical Physics* **22**, 23929 (2020).

[38] A. D. Kim and M. Widom, Interaction models and configurational entropies of binary MoTa and the MoNbTaW high entropy alloy, *Physical Review Materials* **7**, 063803 (2023).

[39] G. Vazquez, D. Saucedo, and R. Arróyave, Deciphering chemical ordering in High Entropy Materials: A machine learning-accelerated high-throughput cluster expansion approach, *Acta Materialia* **276**, 120137 (2024).

[40] C. Zhang and Y. Yang, The CALPHAD approach for HEAs: Challenges and opportunities, *MRS Bulletin* **47**, 158 (2022).

[41] T. Li, S. Wang, W. Fan, Y. Lu, T. Wang, T. Li, and P. K. Liaw, CALPHAD-aided design for superior thermal stability and mechanical behavior in a TiZrHfNb refractory high-entropy alloy, *Acta Materialia* **246**, 118728 (2023).

[42] P. Singh, A. V. Smirnov, and D. D. Johnson, Atomic short-range order and incipient long-range order in high-entropy alloys, *Physical Review B* **91**, 224204 (2015).

[43] F. Körmann, A. V. Ruban, and M. H. Sluiter, Long-ranged interactions in bcc NbMoTaW high-entropy alloys, *Materials Research Letters* **5**, 35 (2017).

[44] P. Singh, A. V. Smirnov, and D. D. Johnson, Ta-Nb-Mo-W refractory high-entropy alloys: Anomalous ordering behavior and its intriguing electronic origin, *Physical Review Materials* **2**, 055004 (2018).

[45] K. Momma and F. Izumi, *VESTA 3* for three-dimensional visualization of crystal, volumetric and morphology data, *Journal of Applied Crystallography* **44**, 1272 (2011).

[46] S. N. Khan, J. B. Staunton, and G. M. Stocks, Statistical physics of multicomponent alloys using KKR-CPA, *Physical Review B* **93**, 054206 (2016).

[47] C. D. Woodgate and J. B. Staunton, Compositional phase stability in medium-entropy and high-entropy Cantor-Wu alloys from an *ab initio* all-electron Landau-type theory and atomistic modeling, *Physical Review B* **105**, 115124 (2022).

[48] C. D. Woodgate, *Modelling Atomic Arrangements in Multicomponent Alloys: A Perturbative, First-Principles-Based Approach*, Springer Series in Materials Science, Vol. 346 (Springer Nature Switzerland, Cham, 2024).

[49] J. Korringa, On the calculation of the energy of a Bloch wave in a metal, *Physica* **13**, 392 (1947).

[50] W. Kohn and N. Rostoker, Solution of the Schrödinger Equation in Periodic Lattices with an Application to Metallic Lithium, *Physical Review* **94**, 1111 (1954).

[51] H. Ebert, D. Ködderitzsch, and J. Minár, Calculating condensed matter properties using the KKR-Green's function method—recent developments and applications, *Reports on Progress in Physics* **74**, 096501 (2011).

[52] P. Hohenberg and W. Kohn, Inhomogeneous Electron Gas, *Physical Review* **136**, B864 (1964).

[53] W. Kohn and L. J. Sham, Self-Consistent Equations Including Exchange and Correlation Effects, *Physical Review* **140**, A1133 (1965).

[54] R. M. Martin, *Electronic Structure: Basic Theory and Practical Methods* (Cambridge University Press, Cambridge, UK, 2004).

[55] J. S. Faulkner, G. M. Stocks, and Y. Wang, *Multiple Scattering Theory: Electronic Structure of Solids*, 1st ed. (IOP Publishing, Bristol, UK, 2018).

[56] R. J. Elliott, J. A. Krumhansl, and P. L. Leath, The theory and properties of randomly disordered crystals and related physical systems, *Reviews of Modern Physics* **46**, 465 (1974).

[57] P. Soven, Coherent-Potential Model of Substitutional Disordered Alloys, *Physical Review* **156**, 809 (1967).

[58] P. Soven, Application of the Coherent Potential Approximation to a System of Muffin-Tin Potentials, *Physical Review B* **2**, 4715 (1970).

[59] B. L. Györffy, Coherent-Potential Approximation for a Nonoverlapping-Muffin-Tin-Potential Model of Random Substitutional Alloys, *Physical Review B* **5**, 2382 (1972).

[60] G. M. Stocks, W. M. Temmerman, and B. L. Györffy, Complete Solution of the Korringa-Kohn-Rostoker

Coherent-Potential-Approximation Equations: Cu-Ni Alloys, *Physical Review Letters* **41**, 339 (1978).

[61] D. Redka, S. A. Khan, E. Martino, X. Mettan, L. Ceric, D. Tolj, T. Ivšić, A. Held, M. Caputo, E. B. Guedes, V. N. Strocov, I. Di Marco, H. Ebert, H. P. Huber, J. H. Dil, L. Forró, and J. Minár, Interplay between disorder and electronic correlations in compositionally complex alloys, *Nature Communications* **15**, 7983 (2024).

[62] D. Bista, W. B. Beeson, T. Sengupta, J. Jackson, S. N. Khanna, K. Liu, and G. Yin, Fast *ab initio* design of high-entropy magnetic materials, *Physical Review Materials* **9**, L031401 (2025).

[63] G. D. Samolyuk, S. Mu, A. F. May, B. C. Sales, S. Wimmer, S. Mankovsky, H. Ebert, and G. M. Stocks, Temperature dependent electronic transport in concentrated solid solutions of the 3d-transition metals Ni, Fe, Co and Cr from first principles, *Physical Review B* **98**, 165141 (2018).

[64] S. Mu, G. D. Samolyuk, S. Wimmer, M. C. Troparevsky, S. N. Khan, S. Mankovsky, H. Ebert, and G. M. Stocks, Uncovering electron scattering mechanisms in NiFeCoCrMn derived concentrated solid solution and high entropy alloys, *npj Computational Materials* **5**, 1 (2019).

[65] V. Raghuraman, Y. Wang, and M. Widom, An investigation of high entropy alloy conductivity using first-principles calculations, *Applied Physics Letters* **119**, 121903 (2021).

[66] F. Tian, L. Delczeg, N. Chen, L. K. Varga, J. Shen, and L. Vitos, Structural stability of NiCoFeCrAl<sub>x</sub> high-entropy alloy from *ab initio* theory, *Physical Review B* **88**, 085128 (2013).

[67] F. Tian, Y. Wang, and L. Vitos, Impact of aluminum doping on the thermo-physical properties of refractory medium-entropy alloys, *Journal of Applied Physics* **121**, 015105 (2017).

[68] S. Huang, F. Tian, and L. Vitos, Elasticity of high-entropy alloys from *ab initio* theory, *Journal of Materials Research* **33**, 2938 (2018).

[69] A. G. Khachaturyan, Ordering in substitutional and interstitial solid solutions, *Progress in Materials Science* **22**, 1 (1978).

[70] B. L. Györffy and G. M. Stocks, Concentration Waves and Fermi Surfaces in Random Metallic Alloys, *Physical Review Letters* **50**, 374 (1983).

[71] D. D. Johnson, D. M. Nicholson, F. J. Pinski, B. L. Györffy, and G. M. Stocks, Density-Functional Theory for Random Alloys: Total Energy within the Coherent-Potential Approximation, *Physical Review Letters* **56**, 2088 (1986).

[72] D. D. Johnson, D. M. Nicholson, F. J. Pinski, B. L. Györffy, and G. M. Stocks, Total-energy and pressure calculations for random substitutional alloys, *Physical Review B* **41**, 9701 (1990).

[73] J. B. Staunton, D. D. Johnson, and F. J. Pinski, Compositional short-range ordering in metallic alloys: Band-filling, charge-transfer, and size effects from a first-principles all-electron Landau-type theory, *Physical Review B* **50**, 1450 (1994).

[74] D. D. Johnson, J. B. Staunton, and F. J. Pinski, First-principles all-electron theory of atomic short-range ordering in metallic alloys: D0<sub>22</sub>- versus L1<sub>2</sub>-like correlations, *Physical Review B* **50**, 1473 (1994).

[75] J. F. Clark, F. J. Pinski, D. D. Johnson, P. A. Sterne, J. B. Staunton, and B. Ginatempo, van Hove Singularity Induced L1<sub>1</sub> Ordering in CuPt, *Physical Review Letters* **74**, 3225 (1995).

[76] C. D. Woodgate, G. A. Marchant, L. B. Pártay, and J. B. Staunton, Structure, short-range order, and phase stability of the Al<sub>x</sub>CrFeCoNi high-entropy alloy: insights from a perturbative, DFT-based analysis, *npj Computational Materials* **10**, 271 (2024).

[77] C. D. Woodgate, H. J. Naguszewski, D. Redka, M. Ján, Q. David, and J. B. Staunton, Emergent B2 chemical orderings in the AlTiVNb and AlTiCrMo refractory high-entropy superalloys studied via first-principles theory and atomistic modelling, *Journal of Physics: Materials* **8**, 045002 (2025).

[78] C. D. Woodgate and J. B. Staunton, Competition between phase ordering and phase segregation in the Ti<sub>x</sub>NbMoTaW and Ti<sub>x</sub>VNbMoTaW refractory high-entropy alloys, *Journal of Applied Physics* **135**, 135106 (2024).

[79] C. D. Woodgate and J. B. Staunton, Short-range order and compositional phase stability in refractory high-entropy alloys via first-principles theory and atomistic modeling: NbMoTa, NbMoTaW, and VNbMoTaW, *Physical Review Materials* **7**, 013801 (2023).

[80] W. L. Bragg and E. J. Williams, The effect of thermal agitation on atomic arrangement in alloys, *Proceedings of the Royal Society of London. Series A, Containing Papers of a Mathematical and Physical Character* **145**, 699 (1934).

[81] W. L. Bragg and E. J. Williams, The effect of thermal agitation on atomic arrangement in alloys-II, *Proceedings of the Royal Society of London. Series A - Mathematical and Physical Sciences* **151**, 540 (1935).

[82] N. Metropolis, A. W. Rosenbluth, M. N. Rosenbluth, A. H. Teller, and E. Teller, Equation of State Calculations by Fast Computing Machines, *Journal of Chemical Physics* **21**, 1087 (1953).

[83] D. P. Landau and K. Binder, *A Guide to Monte Carlo Simulations in Statistical Physics*, 4th ed. (Cambridge University Press, Cambridge, UK, 2014).

[84] F. Wang and D. P. Landau, Efficient, Multiple-Range Random Walk Algorithm to Calculate the Density of States, *Physical Review Letters* **86**, 2050 (2001).

[85] K. Kawasaki, Diffusion Constants near the Critical Point for Time-Dependent Ising Models. I, *Physical Review* **145**, 224 (1966).

[86] H. J. Naguszewski, C. D. Woodgate, and D. Quigley, Optimal parallelisation strategies for flat histogram Monte Carlo sampling, arXiv:2510.11562 .

[87] J. M. Cowley, An Approximate Theory of Order in Alloys, *Physical Review* **77**, 669 (1950).

[88] J. M. Cowley, Short-Range Order and Long-Range Order Parameters, *Physical Review* **138**, A1384 (1965).

[89] K. Sheriff, Y. Cao, T. Smidt, and R. Freitas, Quantifying chemical short-range order in metallic alloys, *Proceedings of the National Academy of Sciences of the United States of America* **121**, e2322962121 (2024).

[90] W. H. Butler, Theory of electronic transport in random alloys: Korringa-Kohn-Rostoker coherent-potential approximation, *Physical Review B* **31**, 3260 (1985).

[91] R. Kubo, Statistical-Mechanical Theory of Irreversible Processes. I. General Theory and Simple Applications to Magnetic and Conduction Problems, *Journal of the*

Physical Society of Japan **12**, 570 (1957).

[92] D. A. Greenwood, The Boltzmann Equation in the Theory of Electrical Conduction in Metals, *Proceedings of the Physical Society* **71**, 585 (1958).

[93] O. K. Andersen, Linear methods in band theory, *Physical Review B* **12**, 3060 (1975).

[94] H. Ebert *et al.*, The Munich SPR-KKR package, <https://sprkrkr.org>.

[95] S. H. Vosko, L. Wilk, and M. Nusair, Accurate spin-dependent electron liquid correlation energies for local spin density calculations: a critical analysis, *Canadian Journal of Physics* **58**, 1200 (1980).

[96] E. Bruno and B. Giner-tempo, Algorithms for Korringa-Kohn-Rostoker electronic structure calculations in any Bravais lattice, *Physical Review B* **55**, 12946 (1997).

[97] H. J. Naguszewski, L. B. Pártay, D. Quigley, and C. D. Woodgate, BraWl: Simulating the thermodynamics and phase stability of multicomponent alloys using conventional and enhanced sampling techniques, *Journal of Open Source Software* **10**, 8346 (2025).

[98] G. M. Stephen, I. McDonald, B. Lejeune, L. H. Lewis, and D. Heiman, Synthesis of low-moment CrVTiAl: A potential room temperature spin filter, *Applied Physics Letters* **109**, 242401 (2016).

[99] Y. Venkateswara, S. Gupta, S. S. Samatham, M. R. Varma, Enamullah, K. G. Suresh, and A. Alam, Competing magnetic and spin-gapless semiconducting behavior in fully compensated ferrimagnetic CrVTiAl: Theory and experiment, *Physical Review B* **97**, 054407 (2018).

[100] G. M. Stephen, C. Lane, G. Buda, D. Graf, S. Kaprzyk, B. Barbiellini, A. Bansil, and D. Heiman, Electrical and magnetic properties of thin films of the spin-filter material CrVTiAl, *Physical Review B* **99**, 224207 (2019).

[101] G. M. Stephen, G. Buda, M. E. Jamer, C. Lane, S. Kaprzyk, B. Barbiellini, D. Graf, L. H. Lewis, A. Bansil, and D. Heiman, Structural and electronic properties of the spin-filter material CrVTiAl with disorder, *Journal of Applied Physics* **125**, 123903 (2019).

[102] J. B. Staunton, D. D. Johnson, and B. L. Győrffy, Interaction between magnetic and compositional order in Ni-rich  $Ni_cFe_{1-c}$  alloys (invited), *Journal of Applied Physics* **61**, 3693 (1987).

[103] C. D. Woodgate, D. Hedlund, L. H. Lewis, and J. B. Staunton, Interplay between magnetism and short-range order in medium- and high-entropy alloys: Cr-CoNi, CrFeCoNi, and CrMnFeCoNi, *Physical Review Materials* **7**, 053801 (2023).

[104] S. Ghosh, K. Ueltzen, J. George, J. Neugebauer, and F. Körmann, Chemical ordering and magnetism in face-centered cubic CrCoNi alloy, *npj Computational Materials* **10**, 284 (2024).

[105] I. Ohnuma, Y. Fujita, H. Mitsui, K. Ishikawa, R. Kainuma, and K. Ishida, Phase equilibria in the Ti-Al binary system, *Acta Materialia* **48**, 3113 (2000).

[106] A. Stukowski, Visualization and analysis of atomistic simulation data with OVITO—the Open Visualization Tool, *Modelling and Simulation in Materials Science and Engineering* **18**, 015012 (2010).

[107] N. Kalliney and M. Widom, X-ray and neutron diffraction patterns of the AlCrTiV high-entropy alloy and quaternary Heusler structures, *Faraday Discussions Advance Article*, 10.1039/D5FD00079C (2026).

[108] G. Samolyuk, A. Shyam, and M. Yoon, A first principles approach for determining solute effect on electrical resistivity of Aluminum solid solution, *Scripta Materialia* **274**, 117138 (2026).

[109] H. Thomas, Über Widerstandslegierungen, *Zeitschrift für Physik* **129**, 219 (1951).

[110] S. Lowitzer, D. Ködderitzsch, H. Ebert, P. R. Tulip, A. Marmodoro, and J. B. Staunton, An ab initio investigation of how residual resistivity can decrease when an alloy is deformed, *Europhysics Letters* **92**, 37009 (2010).

[111] H. Fu, D. Chen, X. Cheng, T. Gao, and X. Yang, The influence of the  $X$  atoms and Al 3p occupied states in AlTi $X_2$  ( $X$  = Fe, Cu, Co, Ni) intermetallics, *Physica B: Condensed Matter* **388**, 303 (2007).

[112] J. Minár, L. Chioncel, A. Perlov, H. Ebert, M. I. Katsnelson, and A. I. Lichtenstein, Multiple-scattering formalism for correlated systems: A KKR-DMFT approach, *Physical Review B* **72**, 045125 (2005).